Air Phase Entrapment Role in Hydrophobic Particle-Water-Air Mixtures Internal Structure and Density

W. Ma[1] and I. omac[1]

[1] University of California San Diego, Department of Structural Engineering, La Jolla 92093, C.A.

Corresponding author: Ingrid Tomac (itomac@ucsd.edu)

Key Points:

- Post-wildfire mudflows contain hydrophobic particles affecting mixture composition and density
- The strong attraction of hydrophobic particles to air bubbles in water leads to a heterogeneous mixture with significant amounts of air.

Abstract

Post-wildfire mudflows, in which more than half of the solids are sand or smaller, destroy the watershed environment, life, and infrastructures. The surficial soil particles turn hydrophobic due to the deposition of combusted organic matter during wildfires. Initiated by raindrops splash, runoff and erosion grow into devastating mudflows, quickly blasting obstacles on the way, and carrying large boulders and debris. The internal composition of post-wildfire mudflows has recently become of interest, intending to understand better mechanisms and transport differences between post-wildfire mudflows and non-post-wildfire mudflows. This paper shows critical new insights into how the air got entrapped during the early stage of mudflow and how air entrapment affects the properties of post-wildfire mudflows as a mixture of air bubbles, water, and hydrophobic sand. This paper proposes and experimentally investigates a new paradigm in which a significant amount of air remains entrapped in post-wildfire mudflow via hydrophobic-particle-air attraction. The mudflow mixture's internal structure depends on the physical state of small liquid marbles, which are small air bubbles covered by hydrophobic sand particles. This paper quantifies the amount of air trapped under different sand-water volumetric concentrations, the effects of mixing speeds (energy), mixing duration, and sand particle size on the final mudflow internal structure. In addition, this paper proposes an empirical estimation of density reductions due to air entrapment in the mixture during the mixing process.

1 Introduction

Post-wildfire mudflows are devastating natural disasters whose frequency increases with climate change and wildfire events worldwide, including California and the Western US, Pacific West, Canada, Europe, and the Mediterranean. In addition, the severity of fire events is likely to increase in the future for most areas due to an increase in regional temperature and dryness

(Fried et al., 2004; Westerling & Bryant, 2008; Westerling et al., 2011; Abatzoglou & Williams, 2016; Lozano et al., 2017; Wotton et al., 2017; Williams et al., 2019; Dupuy et al., 2020; Goss et al., 2020; Halofsky et al., 2020). Post-wildfire mud- and debris flow differ from most natural mudflows because of fire-induced soil wettability modifications. Wildfires combust organic fuel like plant parts in soil and generate hydrophobic substances that precipitate and coat granular soil particles (DeBano et al., 1979; DeBano, 1981, 1991, 2000a; Neary et al., 2005). The fire-induced hydrophobic soil layer averages between 6 cm and 16 cm reported on burned chaparral lands in southern California in the 1960s (Debano et al., 1967; Savage, 1974; Debano et al., 1976; Debano, 2000a, 2000b; Neary et al., 2005), and has been regularly classified in Burned Area Response (BAER) reports (USDA Forest Service, 2021a, 2021b, 2021c). According to Morell et al. (2021), the 2018 Montecito debris flow eroded at least 550,000 m^3 of sediment, and scour depth was between 0.5 m to 2 m. Therefore, assuming the entire layer of fire-induced hydrophobic soil has been eroded during the flood, a rough estimate is that 3% to 32% of Montecito sediments contain hydrophobic soils. Considering the time factor of the flooding process, this percentage must be higher at the beginning of an erosion event. Although wildfires can also reduce the long-term soil hydrophobicity in rare, naturally highly water-repellent areas (Tessler et al., 2013), this research applies to regions with naturally wettable soil that becomes hydrophobic after wildfire, like the USA's arid southwest.

Post-fire mudflows initiate as shallow slopes when rain erodes burned scars' loose surficial soil layers and subsequently carry debris downhill, endangering lives and properties (Cannon et al., 2001; Cannon et al., 2008; Kean et al., 2019). The field's internal structure and composition of post-wildfire mudflows are difficult to quantify due to their short duration and fast flows, up to 30 km/h (Cui et al., 2018). Limited studies have reported post-wildfire sediment yield, hydraulic recovery, hydrophobic bed role, entrainment into mudflows, and erosion patterns

(Kean et al., 2011; Lamb et al., 2011; Ng et al., 2022; Perkins et al., 2022). For example, the solid volumetric concentration varies and can be as high as 60 % in post-wildfire mudflows and debris flows (Conedera et al., 2003; Cannon et al., 2001; Cannon et al., 2008; Kean et al., 2011; Cui et al., 2018; Lee & Widjaja, 2013). In addition to solids and water, Bull (1963) described for the first time how air entrapment occurs in mudflows. Mudflow traps air from the atmosphere while flowing down the tributary ravines and channels, and existing air from pores in the soil deposits can roll into the mudflow. Bull (1963) postulated that part of the air becomes trapped by mudflow and forms bubble cavities that are qualitatively shown in mudflow deposit images and have different shapes and sizes based on sediment material. Furthermore, mudflows can entrap air when obstacles impact the flow (Song et al., 2021; Garoosi et al., 2022). In addition, the air entrapment rate in a granular flow depends on the gradient of solid velocity and flow thickness (Sheng et al., 2013), enhanced by particle hydrophobicity (Cervantes-Álvarez et al., 2020).

Since wildfires turn surficial soil hydrophobic and dried contents of post-fire mudflows likely contain excess air, this paper investigates micromechanics of hydrophobic particle-air-water mixtures to understand better post-wildfire internal composition, air entrapment mechanisms, and density modifications. While previous research highlighted the importance of solids availability on total air entrapment when grains enter the water, further enhanced by hydrophobicity (Cervantes-Álvarez et al., 2020; Ong et al., 2021), the air entrapment dynamics has not been fully quantified for flowing mixtures. Wang et al. (2016) observed submerged three particle-air bubble detachment mechanisms: centrifugal force on particles due to the rotation of the air bubble about its axis in a vortex, irregular trajectories of the particle-bubble complex under motion, strong oscillation of the bubble surface which expels the particles. Furthermore, although many studies investigate the formation and stability of a single liquid marble, which is an air bubble whose surface is covered with a layer of hydrophobic particles (Bormaschenko,

2011; McHale and Newton, 2011, 2015), as further explained in the Supporting Information S1 – S3, the macro-level effects of particle-bubble interactions and dynamics of liquid marbles formation in a flowing mixture with numerous particles and bubbles are poorly understood. Therefore, this paper aims to quantify experimentally and theoretically how kinetic energy, mixing time, interphase forces and dynamics, phase ratios, and solid particles' physical properties, like size, affect the amount of entrapped air via the liquid marble mechanism during water-particle-air mixing. In addition to mudflows, air entrapment into particle-water slurries is relevant in engineering applications (Suhr et al., 1984; Römkens et al., 1997; Sheng et al., 2013; Tanaka et al., 2019; Cervantes-Álvarez et al., 2020; Dunkerley, 2020; Ong et al., 2021; Garoosi et al., 2022).

2 Methodology

This research focuses on sand mixtures because wildfires do not alter hydrophobicity on cohesive soils like clays but significantly affect sands and gravels in highly erodible areas (Debano, 1981; Huffman et al., 2001). Although post-mudflow reconnaissance typically does not quantify volumes of displaced hydrophobic soils, early-stage mudflows are composed of eroded hydrophobic particles from burned scar surfaces. Specifically, this paper studies how air entrapped by hydrophobic particles changes internal structure composition and density in controlled laboratory conditions. Since previous research shows that laboratory sands can well represent site soils following standard geotechnical procedures (Movasat & Tomac, 2021), this research uses clean sand with small sieve sizes to better understand sand size's role in air entrapment. Although post-mudflow reconnaissance efforts to date missed to identify volumes of displaced hydrophobic soils, this study investigates the worst-case scenario and early-stage mudflows as composed of eroded hydrophobic particles from burned scar surfaces.

Experiments consider three types of sand: sieved 10/16 coarse sand (mean particle diameter: 1.33 mm), sieved 40/50 medium silica sand (mean particle diameter: 0.27 mm), and American Foundry Society (AFS) 50/70 testing Ottawa silica fine sand (mean particle diameter: 0.15 mm). Sand is mixed with blades in a 290-ml volume cup with an overall 75-mm height and a 70-mm diameter. After removing fine dust by washing, the sand is oven-dried for 24 hours at 100 °C, and then submerged in a mixed solution of 10% Triethoxy-n-octylsilane ($C_{14}H_{32}O_3Si$) and 90% isopropyl alcohol by volume for at least 48 hours at room temperature, which builds a hydrophobic coating. After the treatment, hydrophobic sand is washed in water and oven dried. Table 1 summarizes the mean contact angles and water drop penetration times for each type of sand after hydrophobicity treatment and includes hydrophobic soil samples from the fire sites and hydrophilic (untreated) sand. Hydrophobicity classification uses the same method in Bisdom et al. (1993) and Leelamanie et al. (2008). The initial volumetric sand-to-water ratio is determined by measuring the sand weight and using the sand's specific gravity (G_S) to obtain the volume of sand solids. Specific gravity is the ratio of the sand grain density to the density of water. The specific gravity for fine, medium, and coarse sand is measured as 2.65, 2.65, and 2.64, respectively.

Table 1. Mean Contact angles and water drop penetration times for different types of artificial hydrophobic sand, hydrophilic (untreated) sand, and hydrophobic sand from a fire site.

Sand Type	Mean Contact Angle, (°)	Water Drop Penetration Time (s) and Repellency Category
Hydrophobic Soil from Fire Site	112 ± 9.6	> 600 (severely water-repellent)
Artificial Hydrophobic Fine Sand	120 ± 8.1	> 3600 (extremely water-repellent)

Artificial Hydrophobic Medium Sand	112 ± 6.4	> 3600 (extremely water-repellent)
Artificial Hydrophobic Coarse Sand	109 ± 8.9	> 3600 (extremely water-repellent)
Hydrophilic (Normal) Fine Sand	57 ± 2.1	0.08 (Wettable / Non-repellent)
Hydrophilic (Normal) Medium Sand	70 ± 2.8	0.02 (Wettable / Non-repellent)
Hydrophilic (Normal) Coarse Sand	68 ± 3.5	0.02 (Wettable / Non-repellent)

A comprehensive mixing program is performed in controlled laboratory conditions to investigate the extent and forms of entrapped air after mixing. The custom mixing system uses a 1-HP motor and variable-frequency drive (VFD) that controls the speed of the mixer blade. Multi-purpose Synthetic Grease prevents all possible water or air leakages from gaps around the container. Before mixing, a certain amount of sand sits at the bottom of the container, followed by pouring water above the sand layer. Air exists naturally within the hydrophobic sand layer and above the water layer within the container. Supporting Information S5 shows details of the mixing blade and investigates the effect of mixing blade shape. Mixing in a cup and vane system replicates kinetic energy and shear rates in post-wildfire mudflows. The shear rates in approximately 1 m high mudflows, at 30 km/h (8.3 m/s) average mudflow velocity, produce shear rates in the order of tens of s^{-1} in laminar regimes. Using the equivalent energy principle as an alternative approach ensures mixing equivalence of the highly heterogeneous three-phase mixture due to the flow regime and dynamics being erratic in nature due to changes of downhill slopes, slope lengths, and natural obstacles, and thus to a large extent unknown before the experiment. Therefore, the vane and cup mixing speed relates to a possible downhill mixture velocity using the work-energy principle:

$$KE_{translational} = \frac{1}{2}mv^2 \quad (1)$$

where $KE_{translational}$ is the kinetic energy of the mixture mass at a translational motion; m is the mixture mass; and v is the linear velocity of the mixture during a mudflow event. Eqn. 2 defines the rotational kinetic energy in the experiments using the work-energy principle:

$$KE_{rotational} = \frac{1}{2} I \omega^2 \tag{2}$$

where $KE_{rotational}$ is the kinetic energy of the mixture mass at a rotational motion; ω is the angular velocity; and I is the moment of inertia of the mixture. When the mixing blade rotates, the mixture resembles a hollow cylinder shape with a thin boundary layer at the wall edge; thus, I is estimated for a cylindrical container shown in **Fig. 1**. By equating $KE_{translational}$ in Eqn. 1 and $KE_{rotational}$ in Eqn. 2, one can easily obtain the relationship between translational velocity v from the field and angular velocity ω used in experiments as follows:

$$\omega = \sqrt{\frac{mv^2}{I}} \tag{3}$$

The following example demonstrates the calculation: a 30.5-g of fine sand and 218.5-g water mixture, rotating at an angular velocity of 314 rad/s, is subjected to a total rotational energy of 3.84 kg-m^2/s^2. However, when the same mixture mass is subjected to equivalent kinetic energy flowing downhill, it reaches the velocity of 5.6 m/s.

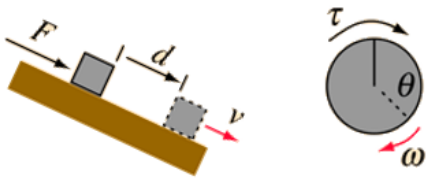

a)

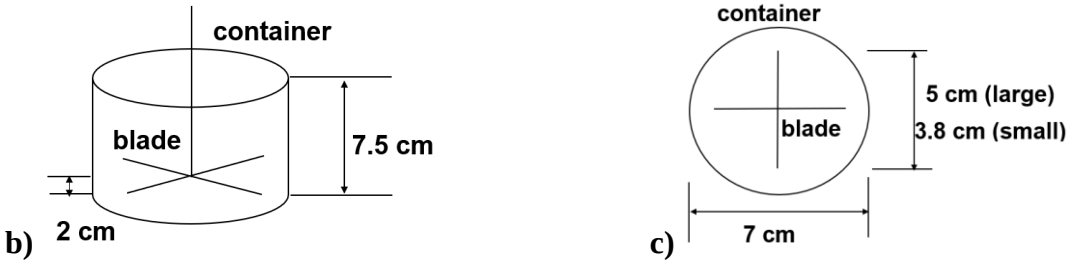

Figure 1. **a)** Relations between downhill velocity and experimental rotational agitation, **b)** Front view and the dimension of the mixing container, **c)** Top view and the dimension of the mixing container

Experiments vary fluid mixing speed, mixing time, and initial solid volumetric concentration of sand (V_s) to the water (V_w) across shear rates, and mixing time varies from 10 s to 120 s. Then, the mixing time increases until evident air-entrapment level changes cease. Depending on how many sand particles are available initially and the type of sand particles, the degas process ends at different times. The degassing process does not change significantly after 60 s for fine sand and after 40 s for medium and coarse sand. The mixing duration stops at 120 s for fine sand, 80 s for medium sand, and 90 s for coarse sand. Before and after mixing, water surface levels help determine the volumes of free air, escaped air, free water, sand particles, and entrapped air. Image documentation of side and top views helps visualize the physical presence and sizes of liquid marbles and sediment.

This paper introduces the specific air content (e^*), the main parameter describing how much air gets entrapped during the mixing process. It is the ratio between the total volume of entrapped air (V_a) to the volume of initial sand particles (V_s):

$$e^* = \frac{V_\mathrm{a}}{V_\mathrm{s}} \tag{4}$$

3 Results

This section summarizes the liquid marble formation process and mechanisms, liquid marble's physical appearance and size estimation after mixing, air entrapment, and final mixture density reduction due to mixing.

3.1 Liquid marble size and stability in post-wildfire mudflows

On a millimeter scale, hydrophobic sand particles have a strong affinity to bond with air, forming a heterogenous mixture with liquid marbles or particle-stabilized air bubbles and preventing degasification (Aussillous and Quéré, 2001; Du et al., 2003; Bormaschenko, 2011; McHale and Newton, 2011, 2015; Ong et al., 2021). Particle attachment, detachment, and collision occur during liquid marble formation (**Figs. 2a-c**). For example, liquid marbles collide; some merge into larger marbles, and others vanish. For example, **Fig. 2a** shows that only a few particles are attached to bubbles within the first 5 s of mixing, and the rest are still floating in the carrying fluid. At 20 s, more sand particles stick to air bubbles (**Fig. 2b**). Finally, particle-covered bubbles collide and form super-large marbles. The initially wide marble size distribution reduces and becomes more uniform after 50-s mixing (**Fig. 2c**).

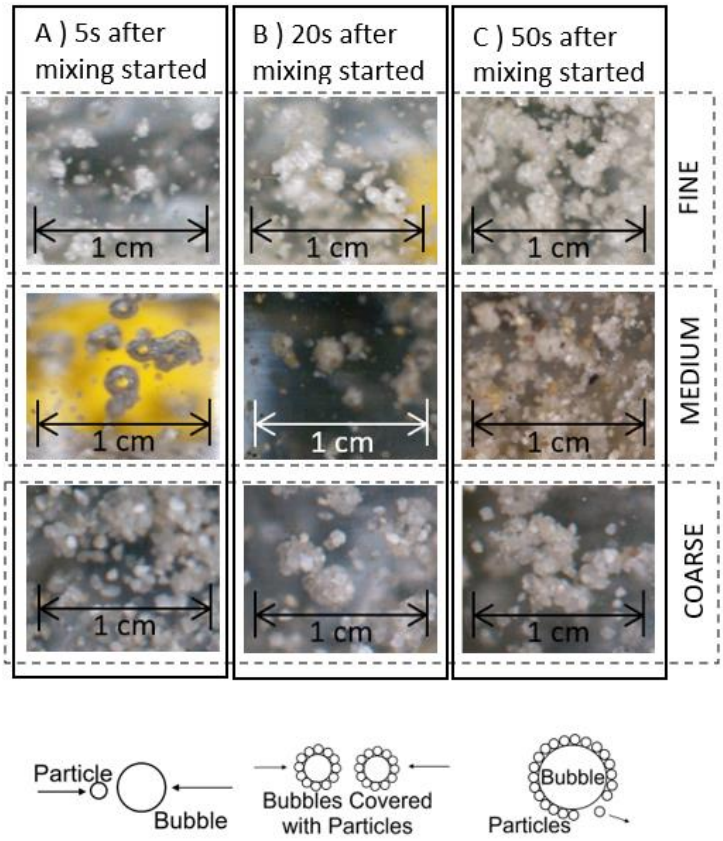

196

197 **Figure 2**. Different sub-processes of particle-bubble interaction include particle bubble
198 approaching, attachment, interactions, and detachment **a)** within the first 5 s, showing a diagram
199 of particle-bubble attachment mechanisms; **b)** within 20 s, showing a diagram of marble-marble
200 collision mechanism; and **c)** within 50 s after mixing started, showing marble-marble collision
201 and particle-bubble separation mechanism.

202

203 This paper theoretically and experimentally investigates the formation process and stability of
204 submerged liquid marbles composed of fine, medium, and coarse hydrophobic sands to
205 understand conditions leading to mudflow air entrapment via liquid marbles. Modified Bond
206 Number (*Bo**) can predict whether liquid marbles will form or not as stable under a specific set
207 of conditions (see Supporting Information, Section S2). Table 2 summarizes the parameters used
208 for calculating *Bo**. Assuming that the blade edge region has the most turbulent fluid flow

condition, the rotation length of a single particle's travel path is taken as the circle circumference that the blade sweeps by. The eddy turbulent accelerations (see Supporting Information, Eqn. S13) have different values since the equivalent downhill mixing velocities are different. **Fig. 3** plots the experimental *Bo** (see Supporting Information, Eqn. S12) for mean particle diameters of each sand with observed average bubble diameters inside liquid marbles that occurred at different mixing speeds against the theoretical *Bo** line at the value of one as a liquid marble stability criterion. Coarser sand particles and higher equivalent downhill mixing speed lead to *Bo** > 1, where liquid marbles become unstable, and particles detach from bubbles more easily.

Table 2. Parameters for calculating the modified Bond number of liquid marbles

	Fine Sand			Medium Sand			Coarse Sand		
Particle Diameter (mm)	0.15			0.27			1.33		
Particle Density (kg/m^3)	2600			2600			2600		
Equivalent downhill mixing velocity (m/s)	3.11	5.44	7.78	3.11	5.44	7.78	3.11	5.44	7.78
Rotating Length Scale (m)	0.157								
Eddy Turbulent Acceleration (m/s^2)	62	188	385	62	188	385	62	188	385
Fluid Surface Tension (N/m)	0.07								
Average Contact Angle (°)	91			91			91		
*Bo**	0.09	0.13	0.18	0.13	0.23	0.40	0.67	1.72	3.34

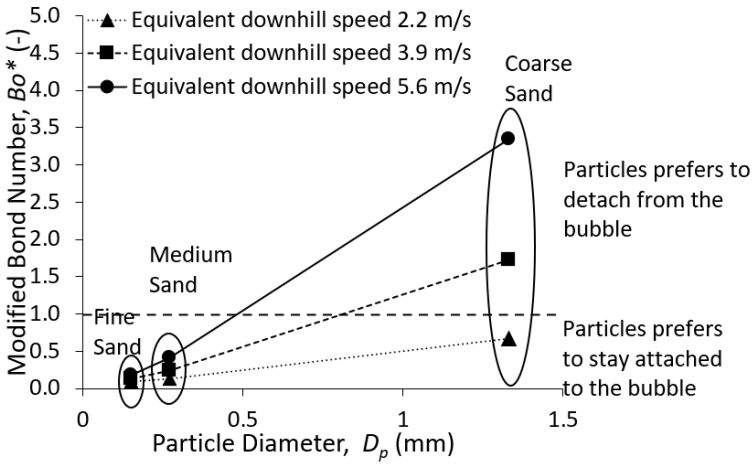

Figure 3. The combined effect of particle diameter D_p and equivalent downhill mixing speed on the modified *Bo**.

Although the modified *Bo** serves as estimate of likelihood in forming liquid marbles during various flow and transport conditions for different sands, the bubble stability estimation based on modified *Bo** has several limitations. First, the modified *Bo** only considers a particle at the bottom of the bubble. Second, *Bo** does not provide information about the liquid marble's size or shape. Third, air pressure and hydrodynamic pressure on the bubble are neglected, while Eqn. S2 (in Supporting Information) provides a more accurate calculation for balancing air pressure and hydrodynamic pressure. Fourth, the particle buoyancy exists at the partially submerged condition, so the approximation using a fully submerged condition is limited, and Eqn. S3 (in Supporting Information) addresses the issue. Fifth, the particle diameter is relatively restricted to a small range: between 0.15 mm and 0.25 mm for fine sand, between 0.25 mm and 0.425 mm for medium sand, and between 1.18 mm and 1.70 mm for coarse sand. The soil in field conditions has a continuous particle diameter distribution of less than 0.075 mm up to 5 mm or above. Lastly, hydrodynamic drag is omitted. Therefore, a comprehensive analysis should

provide a better estimate of liquid marble stability using modified forces and considering multiple particle-bubble locations and a complete set of forces.

Next, the applicability of theoretical Eqns. S14 - S16 (see Supporting Information, section S3) to mudflow conditions liquid marbles is investigated in **Fig. 4**. For fine sand, theoretically-predicted liquid marble diameters are 0.87 mm, 0.75 mm, and 0.45 mm, respectively, based on Eqns. S14-S16 (see Supporting Information). Similarly, for medium sand particles, the liquid marble diameters are 1.57 mm, 1.36 mm, and 1.49 mm, respectively. Finally, the liquid marble diameters for coarse sand particles are 7.72 mm, 6.69 mm, and 7.30 mm, respectively. **Fig. 4** shows positive analysis results for only a high shear rate of 778 s^{-1} where the sand particle size strongly correlates with the final size of liquid marbles, where coarser hydrophobic sand leads to larger marbles. **Fig. 4** results are selected among various tested mixing times, equivalent downhill mixing speeds, and initial solid volumetric concentrations.

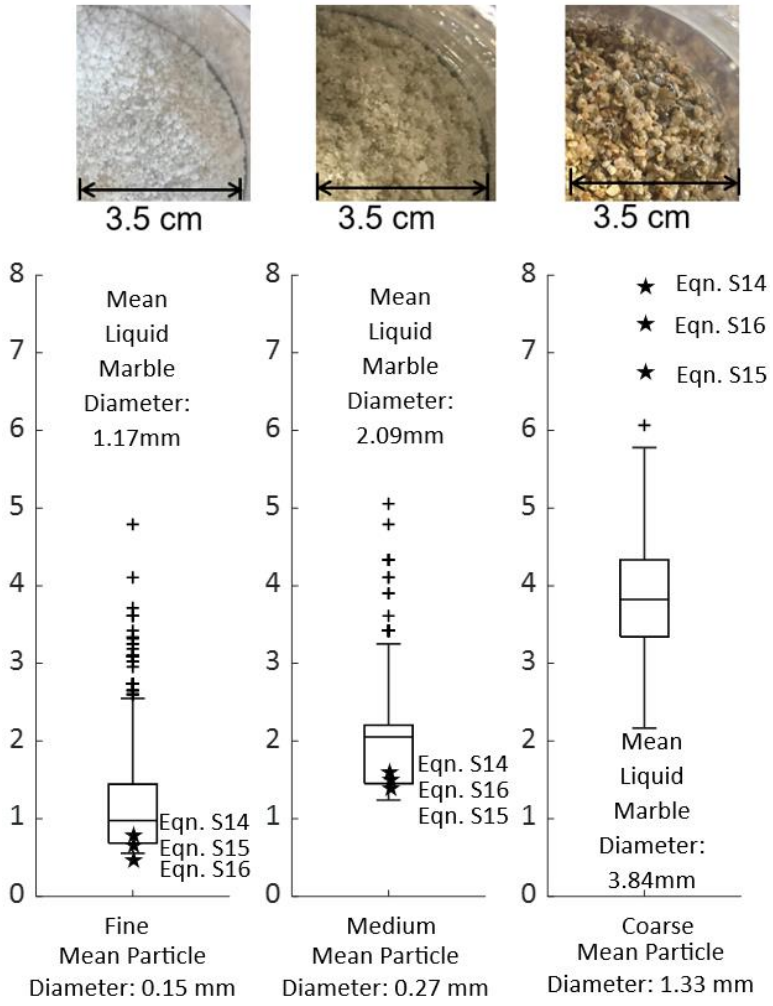

Figure 4. Effect of the sand particle size on the liquid marble size. The results include all initial solid concentrations at the high end of 778 s^{-1}, which produces the most stable liquid marbles. The mixing time is cut after the equilibrium condition: > 60 s for fine sand and > 40 s for medium and coarse sand.

Since *Bo** and Eqns. S14 – S16 are limited in the prediction of sizes and stabilities of liquid marbles in mudflows, a comprehensive force analysis is proposed to identify a full set of conditions in liquid marble formations for post-wildfire mudflow-like mixtures. The analysis quantifies the forces that affect liquid marble formation and uses static and dynamic equilibrium

to understand better liquid marble stability constrained to post-wildfire mudflow conditions. Since a single hydrophobic sand particle can attach to a bubble anywhere on the surface, different scenarios that can be used to study force balance are investigated. In **Fig. 5a,** a hydrophobic sand particle stays at the top of the bubble; in **Fig. 5b,** a particle stays at the left/right side of the bubble, which is the worst-case scenario considering the hydrodynamic effects in horizontal fluid flow; and in **Fig. 5c** a particle stays at the bottom of the bubble which is not favorable when gravity dominates over inertial forces.

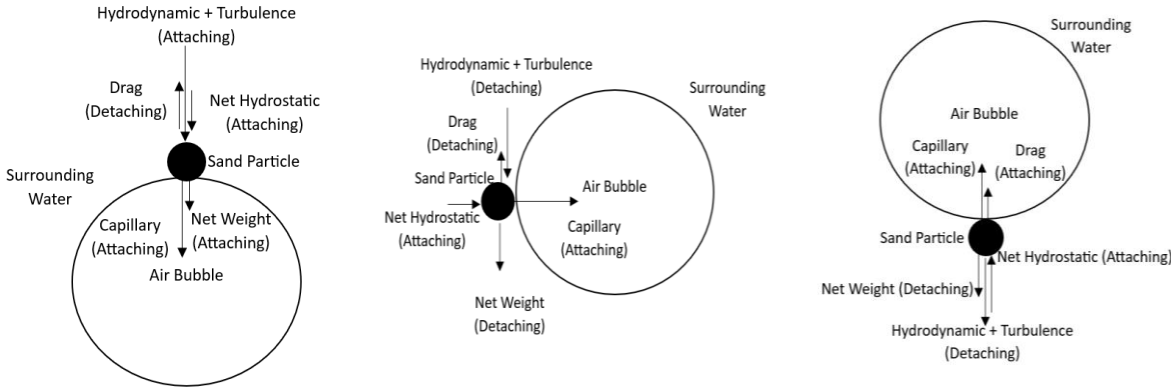

Figure 5. Examples of Forces under different scenarios with different particle-bubble relative locations: **a)** sand particle on the top of the bubble, **b)** sand particle to the left of the bubble, and **c)** sand particle at the bottom of the bubble.

Many forces are involved in particle-bubble interaction (see Supporting Information, Eqns. S1-S11). Three types of static forces dominate in the particle-bubble interaction process (**Fig. 6a**): capillary force, excess force, and net weight force. Capillary force favors particle-bubble attraction (Tao, 2005) and linearly depends on the sand particle diameter (**Fig. 6a**). The excess force acts as an attractive force when the bubble diameter is smaller than 5.5 mm (Tao,

2005) and is a function of the sand particle diameter squared as shown by Eqn. S2 (see Supporting Information). Smaller bubbles experience stronger attractive net hydrostatic forces. The net weight is generally a repulsive force (Tao, 2005). The net weight force (**Fig. 6a**) has a cubic relationship with the sand particle diameter since both the weight and buoyancy parts of the equation depend on the sand particle volume. For all three forces, Young's contact angle applies. Two major hydrodynamic forces exist in the particle-bubble interaction process: hydrodynamic drag force (**Fig. 6b**) and local turbulence force (**Figs. 6e-g**). In drag calculation here, an estimate of drag reduction of 25% is applied. Hydrodynamic drag force is a repulsive force (Tao, 2005). Drag force is linearly dependent on fluid velocity (**Fig. 6b**). The undisturbed fluid flow velocity is assumed to be the same as the velocity provided by the impeller. The particle slip velocity is obtained from Stokes' rule. The drag force is larger on coarser particles.

Reynolds number of the fluid flow during the mixing process is a function of impeller diameter, liquid density, liquid dynamic viscosity, and velocity provided by the impeller (Paul et al., 2004). The mixing process becomes turbulent when the Reynolds number exceeds 10,000 (Paul et al., 2004), which occurs at impeller velocities higher than 4 m/s in this experiment. Therefore, the local turbulence force is only considered in a turbulent flow regime. Flow direction allows hydrodynamic force on particles to attach or detach from the bubble (**Figs. 6c-d**). Instead of plotting hydrodynamic force only, this figure plots the ratio between hydrodynamic force and the sum of all other static forces. The calculation takes the air bubble as a fixed reference point. Therefore, the u_{pb} is the relative velocity between the sand particle and the bubble. The particle velocity is induced by surrounding fluid obtained from Eqns. S4-S9 (see Supporting Information). In case 1 defined in **Fig. 5a**, the sand particle is above the air bubble (hydrodynamic force analysis in **Fig. 6c**). Therefore, net weight, capillary, and excess forces attach forces in which the overall acting direction is downward. When hydrodynamic impact

angle α equals 0 or 2π, the flow direction is parallel to gravity or the overall acting direction of all static forces. When α equals π, the flow direction is perpendicular to gravity. When the hydrodynamic drag force has the same direction as the overall acting direction of all static forces ($0 < \alpha < \pi/2$, or $3\pi/2 < \alpha < 2\pi$), a more attaching particle-bubble interaction will occur. When hydrodynamic drag force is in the opposite direction of the overall acting direction of all static forces ($\pi/2 < \alpha < 3\pi/2$), a detaching particle-bubble interaction will occur. In case 2 defined in **Fig. 5c**, the sand particle is below the air bubble (hydrodynamic force analysis in **Fig. 6d**). Therefore, net weight has a detaching effect, while capillary and excess forces have an attaching effect. The overall acting direction of all static forces is still towards the bubble center (upward, favoring attractive interaction). The hydrodynamic effect is opposite to case 1. While the hydrodynamic impact angle is between $3\pi/2$ and 2π, the hydrodynamic drag force has an attaching effect in particle-bubble interaction. Otherwise, the hydrodynamic drag force causes the detaching effect. The analysis considers local turbulence force an additional enhancement of hydrodynamic drag force. In the force equilibrium analysis, the local turbulence force only applies when the impeller-induced Reynolds number exceeds 10,000. **Figs. 6e-g** show how local turbulent force depends on bubble diameter, sand particle diameter, and fluid energy dissipation. As bubble size increases, the local turbulence force decreases. However, local turbulence force increases as sand particle diameter or fluid energy dissipation increases.

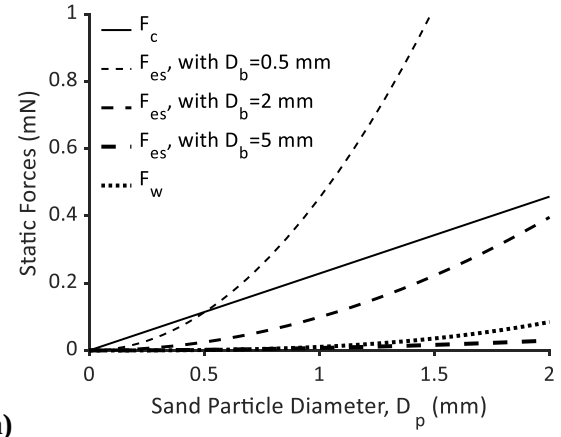
Static Forces (mN)
Sand Particle Diameter, D p (mm)
F c
F es, with D b=0.5 mm
F es, with D b=2 mm
F es, with D b=5 mm
F w

a)

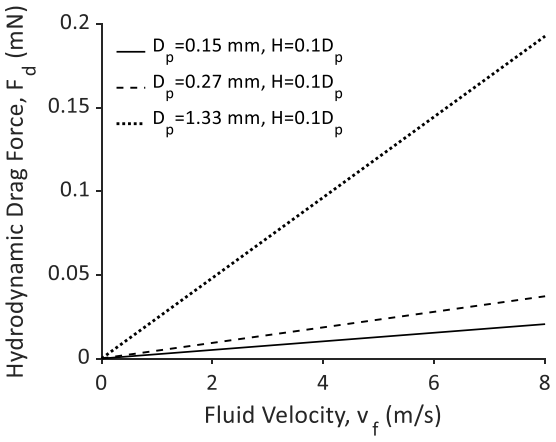
Hydrodynamic Drag Force, F d (mN)
Fluid Velocity, v f (m/s)
D p=0.15 mm, H=0.1D p
D p=0.27 mm, H=0.1D p
D p=1.33 mm, H=0.1D p

b)

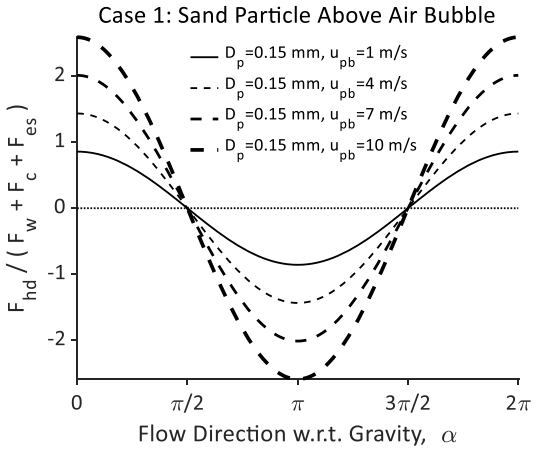
Case 1: Sand Particle Above Air Bubble
F hd / (F w + F c + F es)
Flow Direction w.r.t. Gravity, α
D p=0.15 mm, u pb=1 m/s
D p=0.15 mm, u pb=4 m/s
D p=0.15 mm, u pb=7 m/s
D p=0.15 mm, u pb=10 m/s

c)

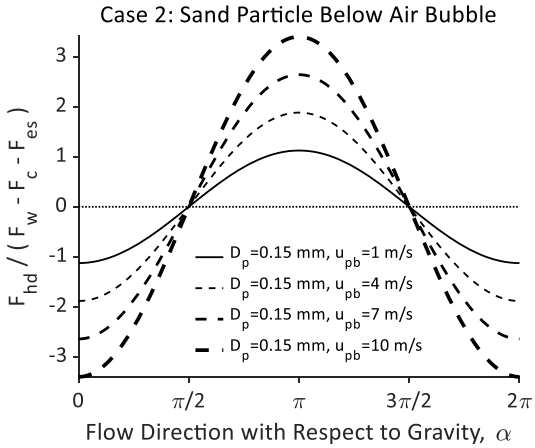
Case 2: Sand Particle Below Air Bubble
F hd / (F w - F c - F es)
Flow Direction with Respect to Gravity, α
D p=0.15 mm, u pb=1 m/s
D p=0.15 mm, u pb=4 m/s
D p=0.15 mm, u pb=7 m/s
D p=0.15 mm, u pb=10 m/s

d)

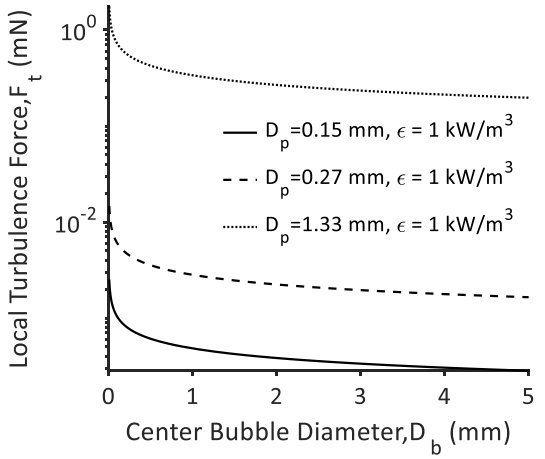
Local Turbulence Force,F t (mN)
Center Bubble Diameter,D b (mm)
D p=0.15 mm, ϵ = 1 kW/m3
D p=0.27 mm, ϵ = 1 kW/m3
D p=1.33 mm, ϵ = 1 kW/m3

e)

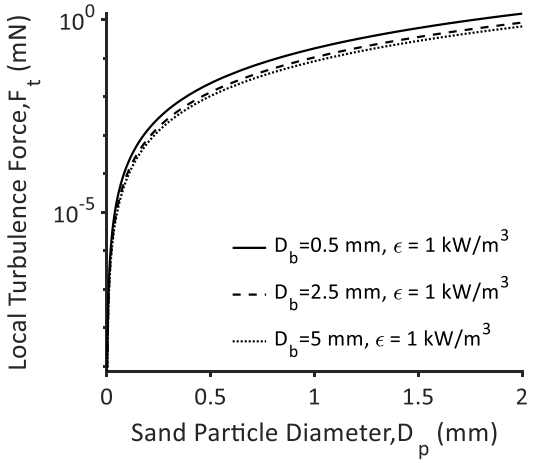
Local Turbulence Force,F t (mN)
Sand Particle Diameter,D p (mm)
D b=0.5 mm, ϵ = 1 kW/m3
D b=2.5 mm, ϵ = 1 kW/m3
D b=5 mm, ϵ = 1 kW/m3

f)

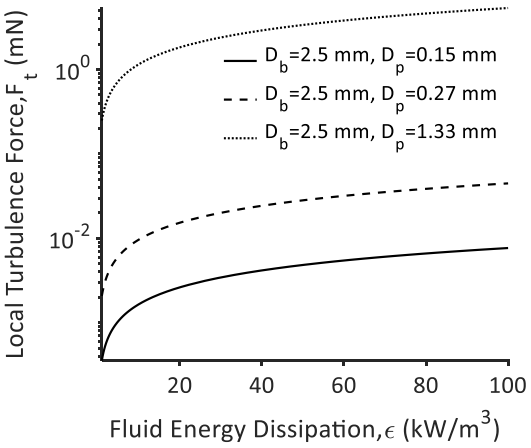

g)

Figure 6. Static and Dynamic forces in particle bubble interaction process. **a)** capillary, excess static, and weight forces, where D_b is the bubble diameter. **b)** hydrodynamic drag forces. **c)** effect of hydrodynamic impact angle when the particle is above the bubble, **d)** effect of hydrodynamic impact angle when the particle is below the bubble, **e)** local turbulence force due to the effect of bubble diameter, **f)** local turbulence force due to the effect of sand particle diameter, **g)** local turbulence force due to the effect of fluid energy dissipation.

Figs. 7a-c quantify results of force balance analysis between capillary, net hydrostatic, hydrodynamic, and local turbulence forces. The shear rate and bubble diameter relationship at a condition of a stable liquid marble, specifically for a single-bubble-single-particle interaction process, is obtained from the force equilibrium. The system is turbulent for all three sand sizes when the particle shear rate exceeds 400 s^{-1} and laminar when the particle shear rate is less than 400 s^{-1}. The cutoff bubble diameter for the analysis is 5.5 mm.

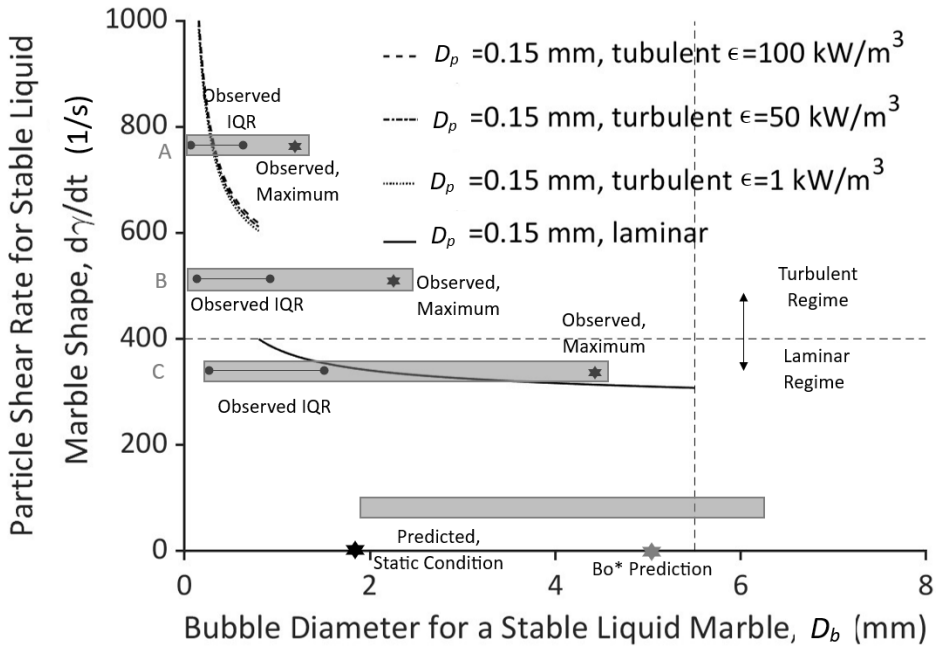
Particle Shear Rate for Stable Liquid Marble Shape, dγ/dt (1/s)
Bubble Diameter for a Stable Liquid Marble, D_b (mm)
D_p =0.15 mm, tubulent ϵ=100 kW/m^3
D_p =0.15 mm, turbulent ϵ=50 kW/m^3
D_p =0.15 mm, turbulent ϵ=1 kW/m^3
D_p =0.15 mm, laminar
Observed IQR
Observed, Maximum
A
B
C
Turbulent Regime
Laminar Regime
Predicted, Static Condition
Bo* Prediction
1000
800
600
400
200
0
0
2
4
6
8

a)

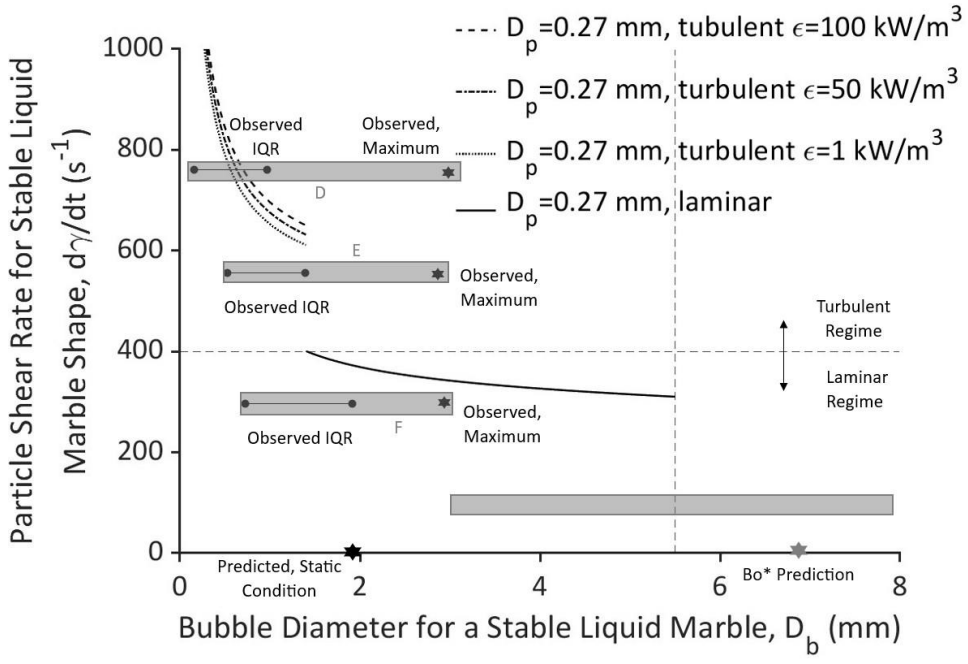
Particle Shear Rate for Stable Liquid Marble Shape, dγ/dt (s^{-1})
Bubble Diameter for a Stable Liquid Marble, D_b (mm)
D_p=0.27 mm, tubulent ϵ=100 kW/m^3
D_p=0.27 mm, turbulent ϵ=50 kW/m^3
D_p=0.27 mm, turbulent ϵ=1 kW/m^3
D_p=0.27 mm, laminar
Observed IQR
Observed, Maximum
D
E
F
Turbulent Regime
Laminar Regime
Predicted, Static Condition
Bo* Prediction
1000
800
600
400
200
0
0
2
4
6
8

b)

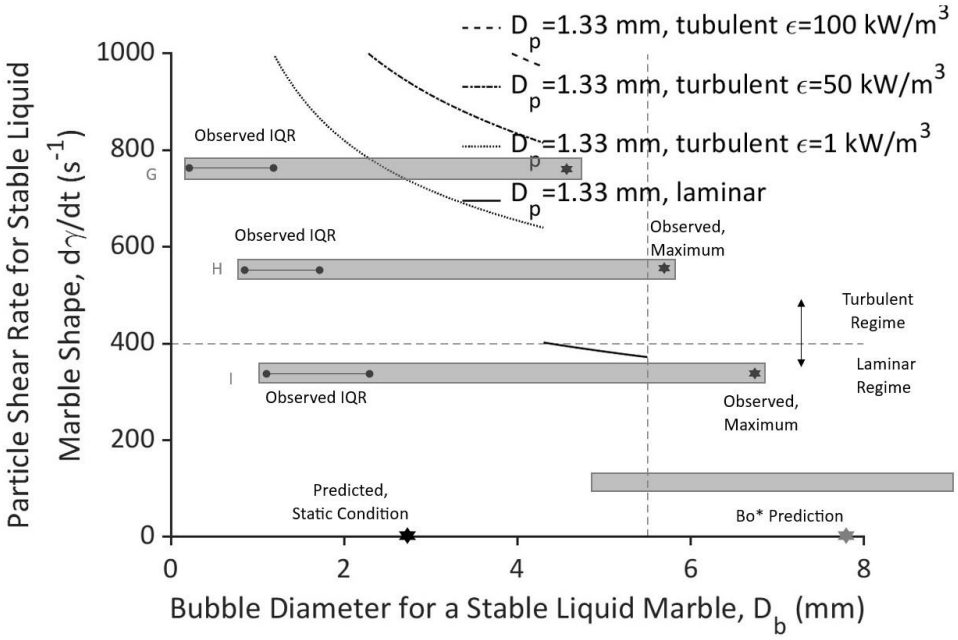

c)

Figure 7. Particle shear rate vs. bubble diameter for a stable liquid marble (single-particle-single-bubble interaction) based on force equilibrium analysis: **a)** fine sand particles, **b)** medium sand particles, **c)** coarse sand particles.

Liquid marbles covered with fine sand particles (**Fig. 7a**) have the largest stable diameter range between 1 and 5.5 mm in a laminar environment among all three types of sand. The analysis (see star dots on the x-axis in Figs. 9a-c) predicts a stable liquid marble diameter of about 1.8 mm using the same forces equations but without the hydrodynamic effect. With a fixed mixing time and a fixed initial solid volumetric concentration ratio, the interquartile range (IQR, or middle 50% and is defined as the difference between the 75% and 25% of the data) of observed liquid marble completely falls below the equilibrium-analysis predicted line for the lowest shear rate of 311 s^{-1} (Cup A, also in **Fig. 8a**). However, the maximum observed liquid marble diameter falls to the right side of the prediction curve. For higher shear rates of 544 s^{-1}

(Cup B, also in **Fig. 8b**) and 778 s^{-1} (Cup C, also in **Fig. 8c**), the IQR of observed liquid marbles will cross the prediction curve further away. Note that the maximum observed liquid marble diameters both fall to the right side of the curve. For liquid marbles covered with medium sand particles (**Fig. 7b**), the range of stable bubble diameter in a laminar environment is narrower, from 1.5 to 5.5 mm. The stable bubble diameter range is smaller for medium sand compared with fine sand conditions. Without a hydrodynamic effect, the stable liquid marble has a predicted bubble diameter of about 1.9 mm. The liquid marble diameter under three different shear rates for medium sand particles is similar to the cases for fine sand particles. The only difference is that the maximum observed liquid marble diameter under the shear rate of 311 s^{-1} (Cup D, also in **Fig. 8d**) is still within the curve boundary. However, it is very close to the boundary. Observed liquid marble diameters exceed the prediction limit for shear rates at 544 s^{-1} (Cup E, also in **Fig. 8e**) and 778 s^{-1} (Cup F, also in **Fig. 8f**). For liquid marble covered with coarse sand particles (**Fig. 7c**), the range of stable bubble diameter in a laminar environment is the shortest, from 4 to 5.5 mm. The stable bubble diameter range is the smallest for coarse sand. That means the liquid marble stability is the worst for coarse sand among all three types of sand particles. Without hydrodynamic effects, the stable liquid marble has a predicted bubble diameter of about 2.6 mm. The IQR of the observed liquid marble still falls within the prediction limit. However, unlike the other two types of sand particles, the maximum observed liquid marbles all fall to the right side of the prediction curve (Cup G, also in **Fig. 8g**; Cup H, also in **Fig. 8h**; Cup I, also in **Fig. 8i**). Overall force equilibrium analysis and experimental data match well, where experimental data show a range of liquid marble diameters. Roughly 70% of the Interquartile Range (IQR) of observed liquid marbles falls within the prediction, meaning most of the liquid marbles obtained from the experiment still follow the general principle of force balances for single-particle-single-bubble interaction. Multiple-particle-single-bubble interaction (Wang et al., 2022) and liquid-

marble-liquid-marble interaction (Jin et al., 2018), particle diameter discrepancies due to sieve sizes, roundness, and sphericity variances are the possible reasons for the observed ranges.

For fine sand particles with an average diameter of 0.15 mm, the average estimated bubble diameter of the final liquid marble covered by fine sand is about 0.96 mm using the force balance method and the three direct estimation equations (see Supporting Information, Eqns. S14-S16) mentioned previously in this paper. Therefore, the collision efficiency (see Supporting Information, Eqn. S17) for a single fine sand particle to collide with a bubble is 0.47. Medium sand particles have an average diameter of 0.27 mm. The average estimated bubble diameter of the final liquid marble covered by medium sand is about 1.33 mm. Thus, the collision efficiency for a single medium sand particle to collide with a bubble is 0.61. Coarse sand particles have an average diameter of 1.33 mm. The average estimated bubble diameter of the final liquid marble covered by coarse sand is about 6.12 mm. The collision efficiency for a single coarse sand particle to collide with a bubble is 0.65.

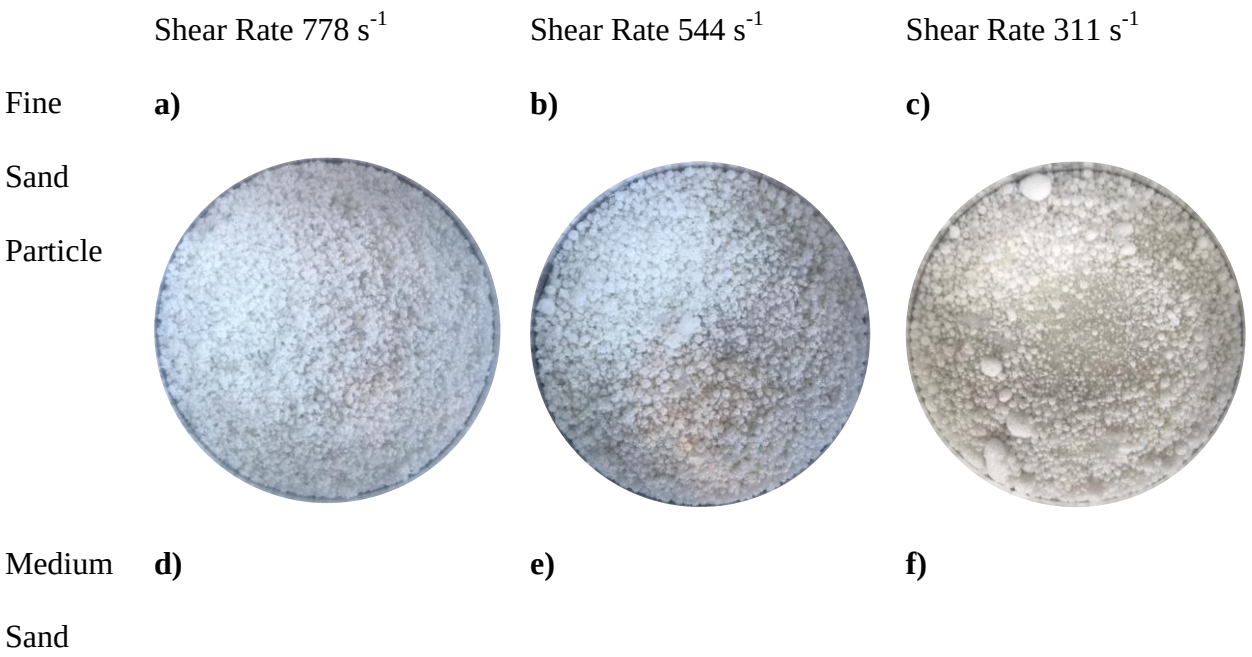

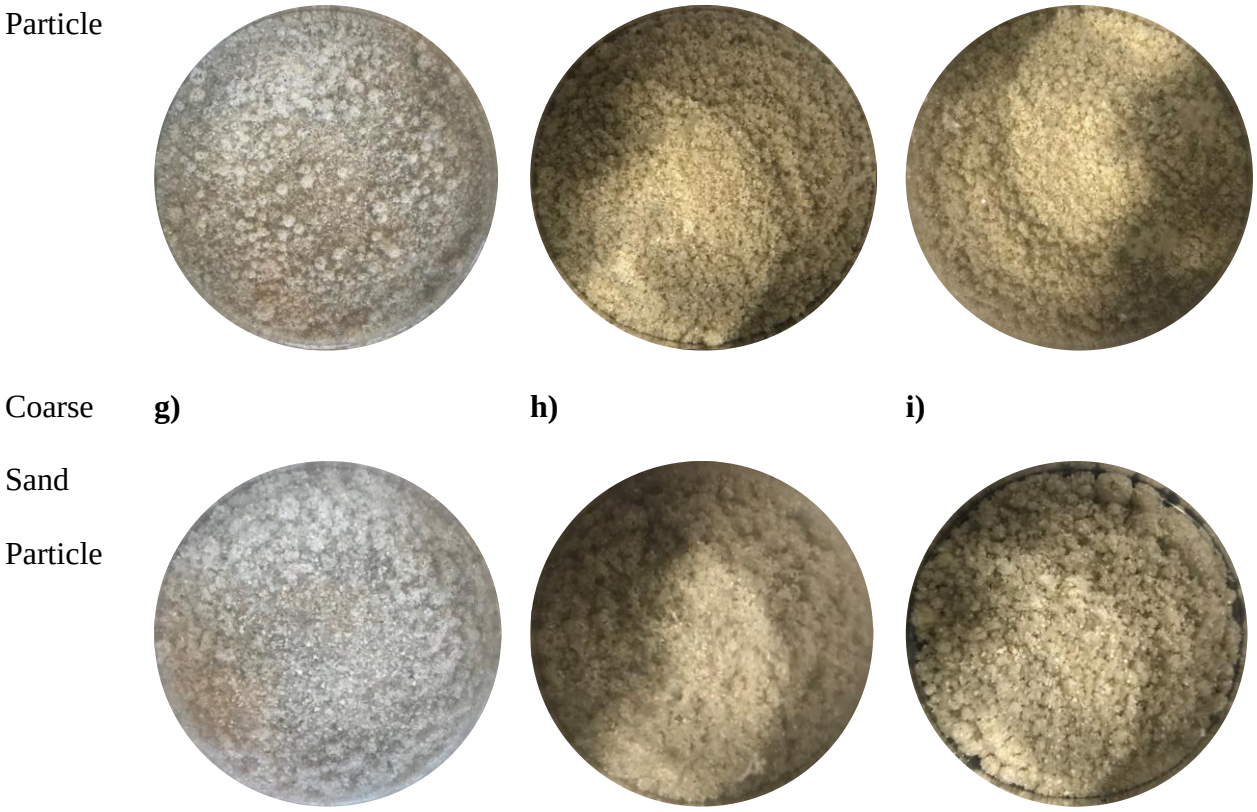

Figure 8. Top Views of Cups A to I in Figure 8.

3.2 Evaluation of the mixture air entrapment and density

The total volume of air trapped in hydrophobic liquid marbles within mixtures is quantified with the specific air content (Eqn. 4), and thus, the bulk density of hydrophobic sand slurries decreases compared to hydrophilic sand slurries. The entrapped air in the three-phase mixture is measured by subtracting the initial water and solid volumes from the total final mixture. The measurement error of volume falls within +/- 1 mL. Table 3 shows a comparison of air entrapments produced with hydrophobic and hydrophilic fine, medium, and coarse sands for a mixing time of 10 – 120 seconds, a shear rate of 311 – 778 s^{-1}, and an initial solid volumetric concentration of 5 – 25%. As introduced at the beginning of the article, debris flows with regular

hydrophilic soil can entrap air bubbles if the debris flow impacts an obstacle (Lugni et al., 2006; Song et al., 2021) or wave surges (Arguden & Rodolfo, 1990); however, it can be seen that hydrophilic sand does not have as strong capability to trap air during the mixing process as hydrophobic sand.

Table 3. A comparison of air entrapment with hydrophobic and hydrophilic sand under selected conditions. V_s is the volume of sand particles, V_w is the volume of water, and e^* is the specific air content.

Sand Particle Type	V_s/V_w	Shear Rates	Mixing Time	e^* for Hydrophilic sand	e^* for Hydrophobic Sand
	(%)	(s^{-1})	(s)	(%)	(%)
Fine	5	778	60	0.0	17
Fine	11	778	60	4.3	22
Fine	18	778	60	2.9	23
Fine	25	778	60	4.3	27
Fine	25	778	10	6.5	70
Fine	25	778	120	4.3	15
Fine	25	544	60	4.3	39
Fine	25	311	60	6.5	49
Medium	5	778	60	0.0	13
Medium	11	778	60	0.0	19
Medium	18	778	60	2.9	20
Medium	25	778	60	4.3	22
Medium	25	778	10	4.3	43
Medium	25	778	80	2.2	18
Medium	25	544	60	4.3	26
Medium	25	311	60	4.3	33
Coarse	5	778	60	0.0	9
Coarse	11	778	60	0.0	12
Coarse	18	778	60	2.9	13
Coarse	25	778	60	2.2	16
Coarse	25	778	10	4.3	48
Coarse	25	544	60	2.2	26
Coarse	25	311	60	4.3	35

Fig. 9 shows the correlation between the specific air content and shear rate. When the shear rate increases, the specific air content decreases. The decreasing behavior of air entrapment changes at around 300 s^{-1}. Before this separating shear rate, air entrapment decreases faster as the shear rate increases. Low mixing power at a low shear rate causes more uneven mixing results, leading to extremely diverse physical appearances of liquid marbles, as shown in **Figs. S4a-b** (see Supporting Information). When mixing at high shear rates, the mixing powers are strong enough to cause a more uniform physical appearance of marbles (**Figs. S4c-f**, see Supporting Information). Hydrodynamic forces from mixing speed must be coupled with other forces, such as resisting forces due to gravity, at low shear rates when investigating their effect on air entrapment. Group "Hydrophobic Fine, V_s/V_w = 11%" provides the range of shear rates to form stable liquid marbles.

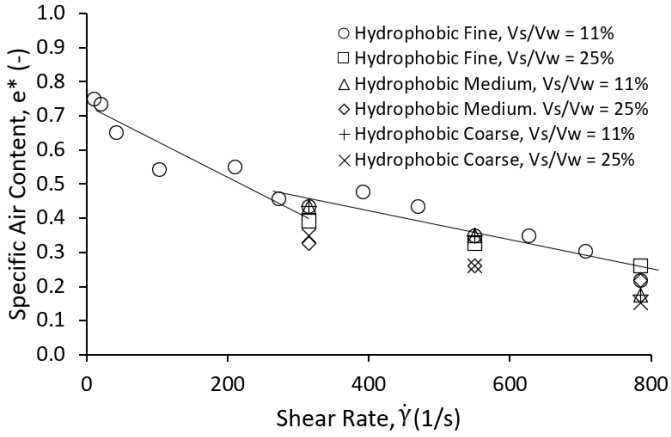

Figure 9. Specific air content vs. shear rate, where all the experiments mixing exceeds 60 seconds.

Fig. 10 further quantifies how the mixing time decreases trapped air aiming towards the equilibrium state by partial degassing. The equilibrium state is defined as the internal structure of

the mixture that is stable against longer and more vigorous mixing, characterized by stable liquid marbles shown in **Fig. S4g** (see Supporting Information). **Figs. 10a-c** show that with smaller diameters and less observable in some cases, liquid marbles form when the mixture undergoes prolonged mixing. It can be seen that coarser sand needs less time to reach the equilibrium, and higher initial solid concentration mixes need a longer time to reach the equilibrium state. **Fig. 10d** synthesizes coupled effects and serves as a base for the proposed empirical relationship:

$$\frac{e^*}{Vs/Vw} = 4.44(tD_p)^{-0.31} \quad (5)$$

Fig. 10e describes an empirical correlation between air entrapment normalized by initial solid volumetric concentration and *Bo**, which depends on the mean particle diameter and mean velocity (see Supporting Information, Eqn. S12). Therefore, besides describing the time effect on the specific air content, this paper proposes another empirical correlation focusing on the velocity effect on the specific air content:

$$\frac{e^*}{\mathrm{V_s}/\mathrm{V_w}} = -0.56 \ln Bo^* + 1.92 \quad (6)$$

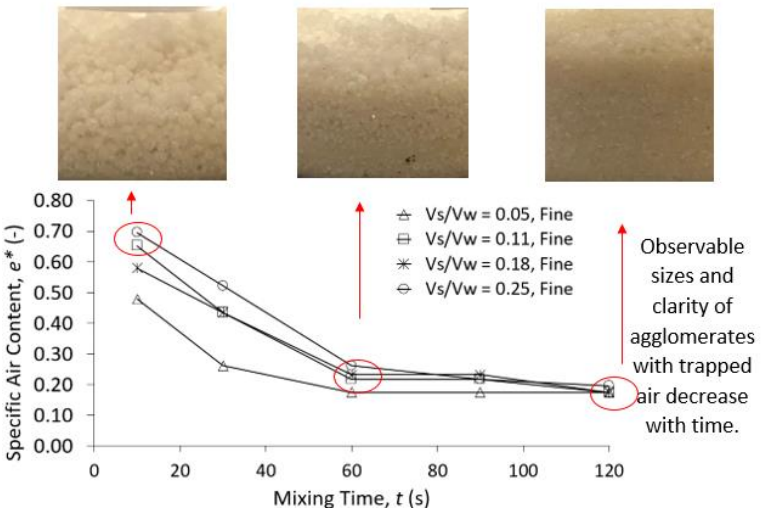

a)

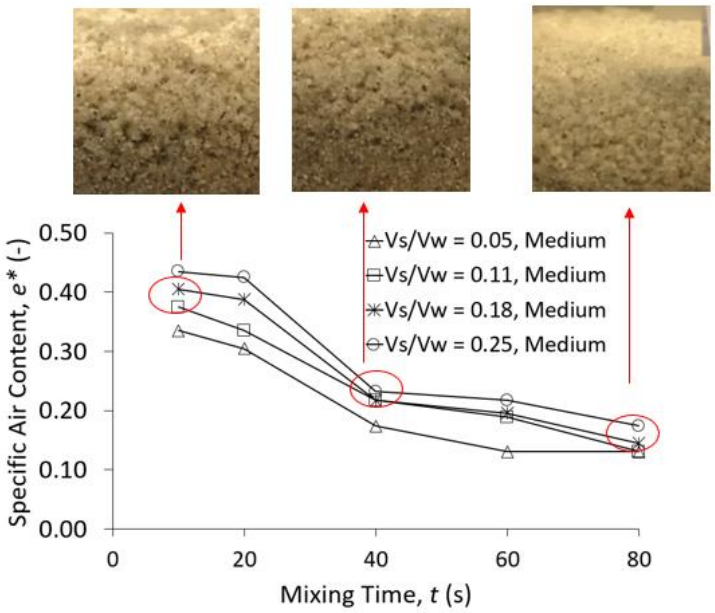
Vs/Vw = 0.05, Medium
Vs/Vw = 0.11, Medium
Vs/Vw = 0.18, Medium
Vs/Vw = 0.25, Medium
Specific Air Content, e* (-)
0.50
0.40
0.30
0.20
0.10
0.00
0
20
40
60
80
Mixing Time, t (s)

441 **b)**

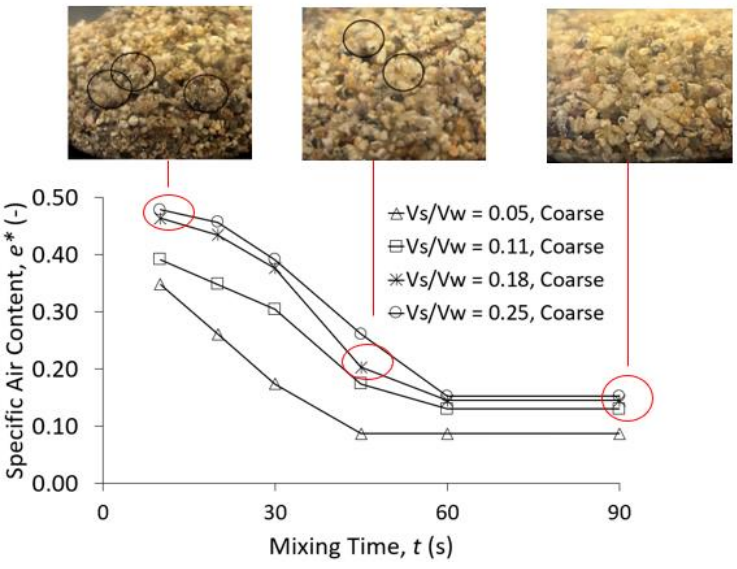
Vs/Vw = 0.05, Coarse
Vs/Vw = 0.11, Coarse
Vs/Vw = 0.18, Coarse
Vs/Vw = 0.25, Coarse
Specific Air Content, e* (-)
0.50
0.40
0.30
0.20
0.10
0.00
0
30
60
90
Mixing Time, t (s)

442 **c)**

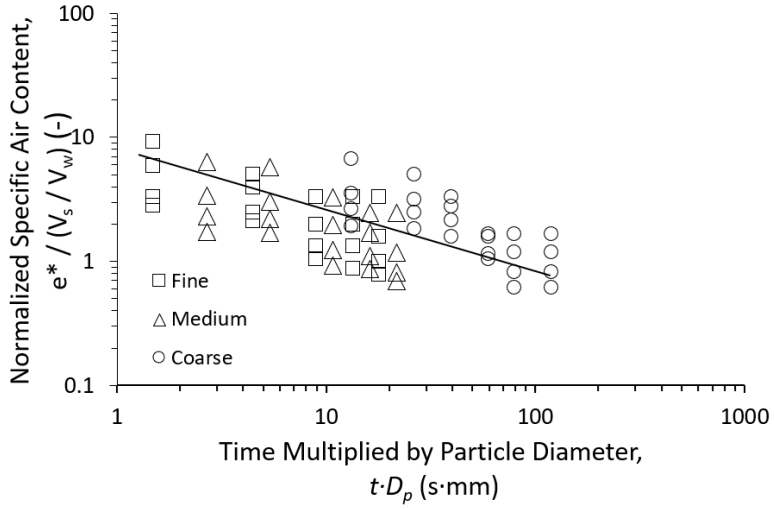

d)

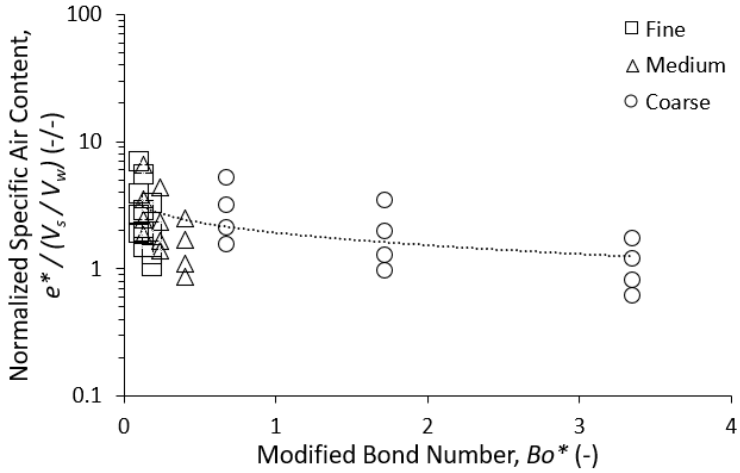

e)

Figure 10. Coupled effect mixing time and types of sand particles on the ability to trap air phase for **a)** fine sand particles, **b)** medium sand particles, **c)** coarse sand particles, and **d)** combined results. **e)** Empirical correlation between specific air content normalized by initial solid volumetric concentration and modified Bond Number.

Besides air entrapment as an essential indicator of the mixing behavior of hydrophobic particles, water, and air, density change before and after mixing is necessary for mudflow models. The density reduction indicates how much water-sand slurry will reduce due to the additional entrapment of air phases when the same amount of sand becomes hydrophobic. **Fig.**

11a shows the effect of mixing time on the density changes of the final mixture. The density reduction will reach a stable condition for the extended mixing time, which is shorter for coarser particles. The average final density reduction is 17%, 13%, and 11% for fine, medium, and coarse sand particles, respectively, when the shear rate is 778 s^{-1} (i.e., the equivalent downhill mixing speed is 7.8 m/s). After ruling out the time effect, shear rate consistently impacts all types of sand (**Fig. 11b**). **Fig. 11b** defines two bounding equations as a speed function to provide a range of estimation of density change normalized by initial solid concentration.

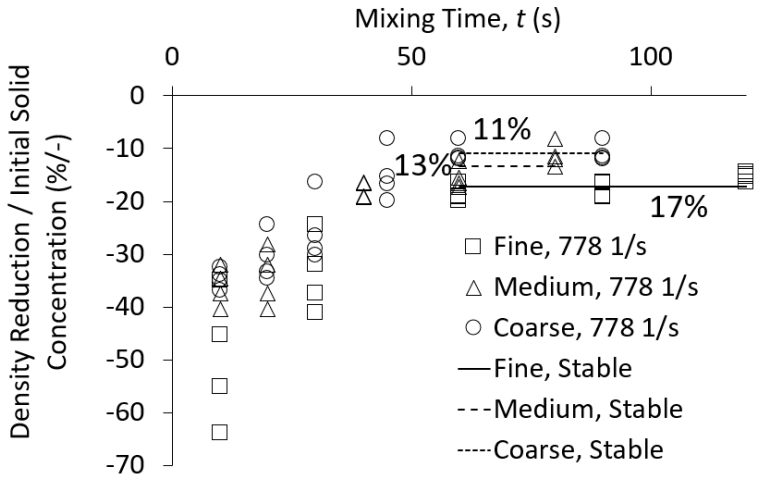

a)

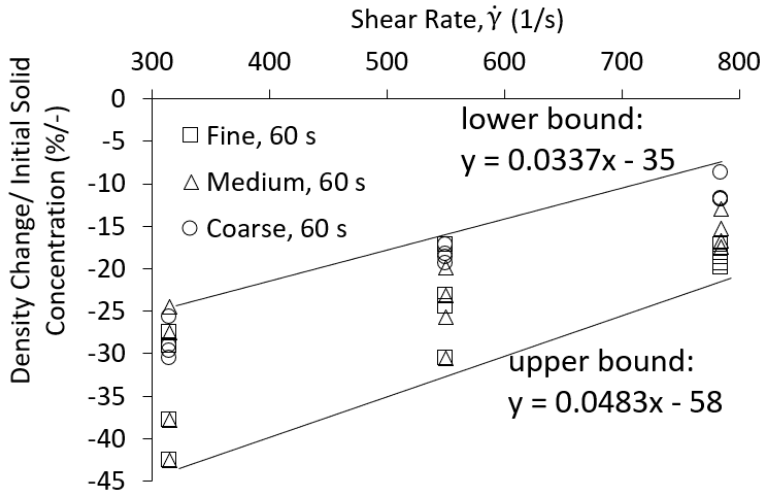

b)

Figure 11. Density reduction due to **a)** mixing time and **b)** shear rate.

4 Discussion and Conclusions

This paper investigated complex mixtures that contain water, hydrophobic sand, and entrapped air. For the first time, this research identified conditions that control air trapping into postwildfire mudflows due to mechanisms enhanced by the wildfire-induced soil hydrophobicity. During wildfires, a surficial layer of non-cohesive sandy soils turns hydrophobic due to the deposition of organic combustion matter on the particle surface. Upon subsequent rain, erosion and mudflows form easily, causing devastating hazards. The air-trapping occurs due to the hydrophobic sand particles attaching to the air bubbles attracted into the mixture, forming liquid marbles in water. This paper shows that sand particles and water are not necessarily only mudflow constituents in hydrophobic slopes because hydrophobic sands have a high capacity to entrap air via liquid marbling mechanisms—an extensive controlled laboratory program aided in understanding liquid marble formation and stability evolution in dense mixtures. The relationship between density change and parameters that can be back-estimated from field analysis, such as average flow velocity in a sloped hill or average solid concentration, have been developed. Fine, medium, and coarse hydrophobic sands represent three different grains of sand as categorized from a geotechnical perspective.

This paper quantified and compared the effects of coupled equivalent downhill mixing speeds, mixing time, sand particle type, and variations in initial air-water-solid volumetric ratios on air entrapment. In addition, the experiments confirm findings from Cervantes-Álvarez et al. (2020), which showed that an initial solid volumetric concentration dominates the final air trapping volume over any other tested factors. Specifically, the initial solid volumetric concentration dominates over shear rates (311 to 778 s^{-1}), shear time (10 to 120 s), and sand particle types (fine, medium, or coarse) in the current study. For the first time, the paper proposes

a forecasting formula for mudflow density for a sand-dominated site under various mixing conditions. Specific new findings show that a longer mixing time gradually decreases the amount of entrapped air. Mixing time affects amount of air and relates to the time from the start rain-induced erosion on burned scar with hydrophobic partices to later times of mudflow dynamics. In addition, mixing time is coupled with the average particle size, and coarser sand needs consistently less mixing time than fine sands to reach a steady volume of trapped air in the mixture at all investigated equivalent downhill mixing speeds. Collision efficiency between a particle and a bubble is higher for coarser sands. Next, considering the mixing rate, air trapped in the mixture decreases as the mixing velocity and sand coarseness increase. Observing air bubbles and liquid marbles can explain the variation and decrease of entrapped air in the mixture under faster, longer mixing and with coarser hydrophobic sands. Coarser sand forms larger liquid marbles than finer sand, with larger modified Bond number, which indicates higher initial bubble shape irregularities where larger marbles deform more and break more easily. Liquid marble breakage is more prominent at a higher speed with a longer mixing time in coarser sand than in other sand. This experiment provides evidence that local turbulence and flow instabilities make particle-bubble interaction more unpredictable and increase the vulnerability of formed liquid marbles toward breakage. As mixing velocity increases, experimental observation deviates more from theoretical calculation. Besides, as mixing velocity increases, larger liquid marbles are hard to survive.

The experiments shown in this paper specialize in narrow particle size to investigate the role of particle size in air entrapment. Although the small-scale mixing experiments in this research are limited compared to site and large-scale soil heterogeneity, they provide an excellent baseline. Experiments show that coarser sand reduces the volume of entrapped air, and with gravel or boulders, air entrapment could be less, because gravity forces from gravels or boulders

and hydrodynamic forces from large particles can easier break the multiphase force balance among air bubbles, water, and solid particles. With less entrapped air and smaller density reduction, the upper bound equation does not change, and the lower bound equation will shift upwards. Since the experiments only consider sand particles, the amount of trapped air could be different if the mixture contains hydrophilic particles and sand, or clays.

Acknowledgments

Financial support provided by the U.S. National Science Foundation, Division of Chemical, Bioengineering, Environmental, and Transport Systems under NSF CBET Grant No. 2025643 is gratefully acknowledged. The authors do not have any conflict of interest. We acknowledge Melisa Lepe for helping with experiments and Haohua Chen and Mahta Movasat for giving constructive feedback on the paper. We thank Haohua Chen for proofreading.

Open Research

Data – Our recorded data, Excel files, and MATLAB code files can be downloaded [https://ingridtomac.eng.ucsd.edu/foldershare/6101].

Software – Analysis and figures were done with Microsoft Excel and MATLAB version R2023a. The MATLAB license is available at: https://mathworks.com/.

References

1. Abatzoglou, J. T. & Williams, A. P. (2016). Impact of anthropogenic climate change on wildfire across western U.S. forests. *Proceedings of the National Academy of Sciences, 113*(42), 11770–11775. https://doi.org/10.1073/pnas.1607171113

2. Arguden, A.T., & Rodolfo, K. S. (1990). Sedimentologic and dynamic differences between hot and cold laharic debris flows of Mayon Volcano, Philippines. *Geological Society of America Bulletin, 102*(7), 865–876. https://doi.org/10.1130/0016-7606(1990)102<0865:saddbh>2.3.co;2
3. Aussillous, P., & Quéré, D., (2001). Liquid marbles. *Nature, 411*(June), 924–927
4. Bisdom, E.B.A., Dekker, L.W., & Schoute, J.F.Th. (1993). Water repellency of sieve fractions from sandy soils and relationships with organic material and soil structure. *Geoderma, 56*(1-4), 105-118. https://doi.org/10.1016/0016-7061(93)90103-R.
5. Bormaschenko, E., (2011). Liquid marbles: Properties and applications. *Current Opinion in Colloid & Interface Scence, 16*(4), 266-271.
6. Bull, W. B. (1963). Alluvial-fan deposits in western Fresno County, California. *The Journal of Geology*, *71*(2), 243–251. https://doi.org/10.1086/626896
7. Cannon, S. H., Gartner, J. E., Wilson, R. C., Bowers, J. C., & Laber, J. L. (2008). Storm rainfall conditions for floods and debris flows from recently burned areas in southwestern Colorado and Southern California. *Geomorphology*, *96*(3-4), 250–269. https://doi.org/10.1016/j.geomorph.2007.03.019
8. Cannon, S. H., Kirkham, R. M., & Parise, M. (2001). Wildfire-related debris-flow initiation processes, Storm King Mountain, Colorado. *Geomorphology*, *39*(3-4), 171–188. https://doi.org/10.1016/s0169-555x(00)00108-2
9. Cervantes-Álvarez, A. M., Escobar-Ortega, Y. Y., Sauret, A., & Pacheco-Vázquez, F. (2020). Air entrainment and granular bubbles generated by a jet of grains entering water. *Journal of Colloid and Interface Science*, *574*, 285–292. https://doi.org/10.1016/j.jcis.2020.04.009

10. Conedera, M., Peter, L., Marxer, P., Forster, F., Rickenmann, D., & Re, L. (2003). Consequences of forest fires on the hydrogeological response of mountain catchments: A case study of the Riale Buffaga, Ticino, Switzerland. *Earth Surface Processes and Landforms, 28*(2), 117–129. https://doi.org/10.1002/esp.425
11. Cui, Y., Cheng, D., & Chan, D. (2018). Investigation of post-fire debris flows in Montecito. *ISPRS International Journal of Geo-Information, 8*(1), 5. https://doi.org/10.3390/ijgi8010005
12. DeBano, L.F., Osborne, J.F., Krammes, J.S., & Letey, L.(1967). Soil wettability and wetting agents … our current knowledge of the problem. USDA Forest Service Research Paper PSW-43, Pacific Southwest Forest and Range Experiment Station, Berkeley, CA
13. DeBano, L.F., Savage, S.M., & Hamilton, D.A. (1976). The transfer of heat and hydrophobic substances during burning. *Soil Science Society of America Journal,* 40, 779-782
14. DeBano, L. F., Rice, R. M., & Eugene, C. C. (1979). Soil heating in chaparral fires: effects on soil properties, plant nutrients, erosion, and runoff. Res. Paper PSW-RP-145. Berkeley, CA: U.S. Department of Agriculture, Forest Service, Pacific Southwest Forest and Range Experiment Station.
15. DeBano, L. F. (1981). Water repellent soils: a state-of-the-art. Gen. Tech. Rep. PSW-GTR-46. Berkeley, CA: U.S. Department of Agriculture, Forest Service, Pacific Southwest Forest and Range Experiment Station.
16. DeBano, L. F. (1991). The effect of fire on soil properties. In: Harvey, Alan E.; Neuenschwander, Leon F., compilers. Proceedings-management and productivity of western-montane forest soils; 1990 April 10-12; Boise, ID. Gen. Tech. Rep. INT-280.

582 Ogden, UT: U.S. Department of Agriculture, Forest Service, Intermountain Research
583 Station.
584 17. DeBano, L. F. (2000a). The role of fire and soil heating on water repellency in Wildland
585 Environments: A Review. *Journal of Hydrology*, *231-232*, 195–206.
586 https://doi.org/10.1016/s0022-1694(00)00194-3
587 18. DeBano, L.F. (2000b). Water repellency in soils: A historical review. *Journal of*
588 *Hydrology, 231-232*, 4-32. https://doi.org/10.1016/S0022-1694(00)00180-3
589 19. Du, Z., Bilbao-Montoya, M.P., Binks, B.P., Dickinson, E., Ettelaie, R., Murray, B.S.
590 (2003). Outstanding Stability of Particle-Stabilized Bubbles. *Langmuir, 19*(8), 3106-
591 3108. https://doi.org/10.1021/la034042n
592 20. Dunkerley, D. (2020). Rainfall intensity in geomorphology: Challenges and
593 opportunities. *Progress in Physical Geography: Earth and Environment*, *45*(4), 488–513.
594 https://doi.org/10.1177/0309133320967893
595 21. Dupuy, J.-L., Fargeon, H., Martin-StPaul, N., Pimont, F., Ruffault, J., Guijarro, M.,
596 Hernando, C., Madrigal, J., & Fernandes, P. (2020). Climate change impact on future
597 wildfire danger and activity in Southern Europe: A Review. *Annals of Forest Science, 77*(2). https://doi.org/10.1007/s13595-020-00933-5
599 22. Fried, J. S., Torn, M. S., & Mills, E. (2004). The impact of climate change on wildfire
600 severity: A regional forecast for Northern California. *Climatic Change, 64*(1/2), 169–191.
601 https://doi.org/10.1023/b:clim.0000024667.89579.ed
602 23. Garoosi, F., Nicole Mellado-Cusicahua, A., Shademani, M., & Shakibaeinia, A. (2022).
603 Experimental and numerical investigations of dam break flow over dry and wet beds.
604 *International Journal of Mechanical Sciences*, *215*, 106946.
605 https://doi.org/10.1016/j.ijmecsci.2021.106946

606 24. Goss, M., Swain, D. L., Abatzoglou, J. T., Sarhadi, A., Kolden, C. A., Williams, A. P., &
607 Diffenbaugh, N. S. (2020). Climate change is increasing the likelihood of extreme
608 autumn wildfire conditions across California. *Environmental Research Letters, 15*(9),
609 094016. https://doi.org/10.1088/1748-9326/ab83a7
610 25. Halofsky, J. E., Peterson, D. L., & Harvey, B. J. (2020). Changing wildfire, changing
611 forests: The effects of climate change on fire regimes and vegetation in the Pacific
612 Northwest, USA. *Fire Ecology, 16*(1). https://doi.org/10.1186/s42408-019-0062-8
613 26. Huffman, E. L., MacDonald, L. H., & Stednick, J. D. (2001). Strength and persistence of
614 fire-induced soil hydrophobicity under ponderosa and Lodgepole Pine, Colorado front
615 range. *Hydrological Processes, 15*(15), 2877–2892. https://doi.org/10.1002/hyp.379
616 27. Jin, J., Ooi, C. H., Dao, D. V., & Nguyen, N.-T. (2018). Liquid marble coalescence via
617 vertical collision. *Soft Matter, 14*(20), 4160–4168. https://doi.org/10.1039/c8sm00121a
618 28. Kean, J. W., Staley, D. M., & Cannon, S. H. (2011). In situ measurements of post-fire
619 debris flows in Southern California: Comparisons of the timing and magnitude of 24
620 debris-flow events with rainfall and soil moisture conditions. *Journal of Geophysical*
621 *Research, 116*(F4). https://doi.org/10.1029/2011jf002005
622 29. Kean, J. W., Staley, D. M., Lancaster, J. T., Rengers, F. K., Swanson, B. J., Coe, J. A.,
623 Hernandez, J. L., Sigman, A. J., Allstadt, K. E., & Lindsay, D. N. (2019). Inundation,
624 flow dynamics, and damage in the 9 January 2018 Montecito Debris-flow event,
625 California, USA: Opportunities and challenges for post-wildfire risk assessment.
626 *Geosphere, 15*(4), 1140–1163. https://doi.org/10.1130/ges02048.1
627 30. Lamb, M. P., Scheingross, J. S., Amidon, W. H., Swanson, E., & Limaye, A. (2011). A
628 model for fire-induced sediment yield by dry Ravel in steep landscapes. *Journal of*
629 *Geophysical Research, 116*(F3). https://doi.org/10.1029/2010jf001878

31. Lee, S. H.-H., & Widjaja, B. (2013). Phase concept for mudflow based on the influence of viscosity. *Soils and Foundations*, *53*(1), 77–90. https://doi.org/10.1016/j.sandf.2012.12.005

32. Leelamanie, D.A.L., Karube, J., Yoshida, A. (2008). Characterizing water repellency indices: Contact angle and water drop penetration time of hydrophobized sand. *Soil Science & Plant Nutrition, 54*(2), 179-187. https://doi.org/10.1111/j.1747-0765.2007.00232.x

33. Lozano, O.M., Salis, M., Ager, A.A., Arca, B., Alcasena, F.J., Monteiro, A.T., Finney, M.A., Del Giudice, L., Scoccimarro, E., & Spano, D. (2017). Assessing climate change impacts on wildfire exposure in Mediterranean areas. *Risk Analysis, 37*, 1898-1916. https://doi.org/10.1111/risa.12739

34. Lugni, C., Brocchini, M., & Faltinsen, O. M. (2006). Wave impact loads: The role of the flip-through. *Physics of Fluids, 18*(12). https://doi.org/10.1063/1.2399077

35. McHale G., and Newton, M.I., (2011). Liquid Marbles: Principles and applications. *Soft Matter, 12*, 5473–5481

36. McHale G., and Newton, M.I., (2015). Liquid Marbles: Topical context within soft matter and recent progress. *Soft Matter, 13*, 2530-2546

37. Morell, K.D., Alessio, P., Dunne, T. and Keller, E., (2021). Sediment Recruitment and Redistribution in Mountain Channel Networks by Post-Wildfire Debris Flows. Geophysical Research Letters, 48(24), p.e2021GL095549.

38. Movasat, M., & Tomac, I. (2021). Assessment of physical properties of water-repellent soils. *Journal of Geotechnical and Geoenvironmental Engineering, 147*(9). https://doi.org/10.1061/(asce)gt.1943-5606.0002604

39. Neary, D. G., Ryan, K. C., & DeBano, L. F. (2005). Wildland fire in ecosystems: effects of fire on soils and water. Gen. Tech. Rep. RMRS-GTR-42-vol.4. Ogden, UT: U.S. Department of Agriculture, Forest Service, Rocky Mountain Research Station.
40. Ng, C. W., Zheng, M., Liu, H., & Poudyal, S. (2022). Effects of bed hydrophobicity on post-fire debris flow entrainment and momentum growth. *Journal of Geophysical Research: Earth Surface, 127*(11). https://doi.org/10.1029/2022jf006783
41. Ong, X. Y., Taylor, S. E., & Ramaioli, M. (2021). On the formation of dry granular jets at a liquid surface. *Chemical Engineering Science*, *245*, 116958. https://doi.org/10.1016/j.ces.2021.116958
42. Paul, E. L., Atiemo-Obeng, V. A., & Kresta, S. M. (2004). *Handbook of Industrial Mixing Science and Practice*. Wiley-Interscience.
43. Perkins, J. P., Diaz, C., Corbett, S. C., Cerovski-Darriau, C., Stock, J. D., Prancevic, J. P., Micheli, E., & Jasperse, J. (2022). Multi-stage soil-hydraulic recovery and limited Ravel accumulations following the 2017 nuns and Tubbs wildfires in Northern California. *Journal of Geophysical Research: Earth Surface, 127*(6). https://doi.org/10.1029/2022jf006591
44. Römkens, M. J. M., Prasad, S. N., & Gerits, J. J. P. (1997). Soil erosion modes of sealing soils: A phenomenological study. *Soil Technology, 11*(1), 31–41. https://doi.org/10.1016/s0933-3630(96)00113-4
45. Savage, S. M. (1974). Mechanism of fire-induced water repellency in soil. *Soil Science Society of America Proceedings, 38*, 652-657
46. Sheng, L. T., Tai, Y. C., Kuo, C. Y., & Hsiau, S. S. (2013). A two-phase model for dry density-varying granular flows. *Advanced Powder Technology*, *24*(1), 132–142. https://doi.org/10.1016/j.apt.2012.04.001

47. Song, D., Chen, X., Zhou, G. G. D., Lu, X., Cheng, G., & Chen, Q. (2021). Impact dynamics of debris flow against rigid obstacle in laboratory experiments. *Engineering Geology*, *291*, 106211. https://doi.org/10.1016/j.enggeo.2021.106211

48. Suhr, J. L., Jarrett, A. R., & Hoover, J. R. (1984). The effect of soil air entrapment on erosion. *Transactions of the ASAE*, *27*(1), 0093–0098. https://doi.org/10.13031/2013.32742

49. Tao, D. (2005). Role of bubble size in flotation of coarse and fine particles—a review. *Separation Science and Technology*, *39*(4), 741–760. https://doi.org/10.1081/ss-120028444

50. Tanaka, Y., Uchida, T., Nagai, H., & Todate, H. (2019). Bench-scale experiments on effects of pipe flow and entrapped air in soil layer on hillslope landslides. *Geosciences*, *9*(3), 138. https://doi.org/10.3390/geosciences9030138

51. Tessler, N., Wittenberg, L., & Greenbaum N. (2013). Soil water repellency persistence after recurrent forest fires on Mount Carmel, Israel. *International Journal of Wildland Fire*, *22*, 515-526.

52. United States Depart of Agriculture Forest Service. (2021a). Monument Fire Burned-Area Report. https://forest.moscowfsl.wsu.edu/BAERTOOLS/baer-db/2500-8/2500-8_Monument_Shasta-Trinity.pdf

53. United States Depart of Agriculture Forest Service. (2021b). McCash Fire Burned-Area Report. https://forest.moscowfsl.wsu.edu/BAERTOOLS/baer-db/2500-8/2500-8_McCash_Six%20Rivers.pdf

54. United States Depart of Agriculture Forest Service. (2021c). French Fire Burned-Area Report. https://forest.moscowfsl.wsu.edu/BAERTOOLS/baer-db/2500-8/2500-8_French_Sequoia.pdf

55. Wang, G., Evans, G. M., & Jameson, G. J. (2016). Bubble–particle detachment in a turbulent Vortex I: Experimental. *Minerals Engineering*, *92*, 196–207. https://doi.org/10.1016/j.mineng.2016.03.011

56. Wang, A., Hoque, M. M., Evans, G., & Mitra, S. (2022). Determining collision efficiency in multi-bubble-particle systems in presence of turbulence. *Minerals Engineering, 189*, 107889. https://doi.org/10.1016/j.mineng.2022.107889

57. Westerling, A. L., Bryant, B. P., Preisler, H. K., Holmes, T. P., Hidalgo, H. G., Das, T., & Shrestha, S. R. (2011). Climate change and growth scenarios for California wildfire. *Climatic Change, 109*(S1), 445–463. https://doi.org/10.1007/s10584-011-0329-9

58. Westerling, A. L., & Bryant, B. P. (2008). Climate change and wildfire in California. *Climatic Change, 87*(S1), 231–249. https://doi.org/10.1007/s10584-007-9363-z

59. Williams, A. P., Abatzoglou, J. T., Gershunov, A., Guzman-Morales, J., Bishop, D. A., Balch, J. K., & Lettenmaier, D. P. (2019). Observed impacts of anthropogenic climate change on wildfire in California. *Earth's Future, 7*(8), 892–910. https://doi.org/10.1029/2019ef001210

60. Wotton, B. M., Flannigan, M. D., & Marshall, G. A. (2017). Potential climate change impacts on fire intensity and key wildfire suppression thresholds in Canada. *Environmental Research Letters, 12*(9), 095003. https://doi.org/10.1088/1748-9326/aa7e6e

References in Supporting Information:

1. Balasubramanian, A. K., Miller, A. C., & Rediniotis, O. K. (2004). Microstructured hydrophobic skin for hydrodynamic drag reduction. AIAA Journal, 42(2), 411–414. https://doi.org/10.2514/1.9104

2. Binks, B. P. & Lumsdon, S. O. (2001). Pickering emulsions stabilized by monodisperse latex particles: effects of particle size. Langmuir, 17(15), 4540–4547. https://doi.org/10.1021/la0103822
3. Brabcová, Z., Karapantsios, T., Kostoglou, M., Basařová, P., & Matis, K. (2015). Bubble particle collision interaction in flotation systems. Colloids and Surfaces A: Physicochemical and Engineering Aspects, 473, 95–103. https://doi.org/10.1016/j.colsurfa.2014.11.040
4. Drzymala, J. (1994). Characterization of materials by Hallimond tube flotation. Part 2: Maximum size of floating particles and contact angle. International Journal of Mineral Processing, 42(3–4), 153–167. https://doi.org/10.1016/0301-7516(94)00035-2
5. Eskanlou, A., Chegeni, M. H., Khalesi, M. R., Abdollahy, M., & Huang, Q. (2019). Modeling the bubble loading based on force balance on the particles attached to the bubble. Colloids and Surfaces A: Physicochemical and Engineering Aspects, 582, 123892. https://doi.org/10.1016/j.colsurfa.2019.123892
6. Fornasiero, D., & Filippov, L. O. (2017). Innovations in the flotation of fine and coarse particles. Journal of Physics: Conference Series, 879, 012002. https://doi.org/10.1088/1742-6596/879/1/012002
7. Fielden, M. L., Hayes, R. A., & Ralston, J. (1996). Surface and capillary forces affecting air bubble−particle interactions in aqueous electrolyte. Langmuir, 12(15), 3721–3727. https://doi.org/10.1021/la960145c
8. Frith, W. J., Pichot, R., Kirkland, M., & Wolf, B. (2008). Formation, stability, and rheology of particle stabilized emulsions: Influence of multivalent cations. Industrial & Engineering Chemistry Research, 47(17), 6434–6444. https://doi.org/10.1021/ie071629e

9. Gai, G., Hadjadj, A., Kudriakov, S., & Thomine, O. (2020). Particles-induced turbulence: A critical review of physical concepts, Numerical Modelings and experimental investigations. Theoretical and Applied Mechanics Letters, 10(4), 241–248. https://doi.org/10.1016/j.taml.2020.01.026
10. Gao, Y., Evans, G. M., Wanless, E. J., & Moreno-Atanasio, R. (2014). DEM simulation of single bubble flotation: Implications for the hydrophobic force in particle–bubble interactions. Advanced Powder Technology, 25(4), 1177–1184. https://doi.org/10.1016/j.apt.2014.05.020
11. Geraldi, N. R., Dodd, L. E., Xu, B. B., Wells, G. G., Wood, D., Newton, M. I., & McHale, G. (2017). Drag reduction properties of superhydrophobic mesh pipes. Surface Topography: Metrology and Properties, 5(3), 034001. https://doi.org/10.1088/2051-672x/aa793b
12. Gillies, G., Kappl, M., & Butt, H.-J. (2005). Direct measurements of particle–bubble interactions. Advances in Colloid and Interface Science, 114-115, 165–172. https://doi.org/10.1016/j.cis.2004.08.003
13. Haney, B., Chen, D., Cai, L.-H., Weitz, D., & Ramakrishnan, S. (2019). Millimeter-size Pickering emulsions stabilized with Janus microparticles. Langmuir, 35(13), 4693–4701. https://doi.org/10.1021/acs.langmuir.9b00058
14. Ishida, N. (2007). Direct measurement of hydrophobic particle–bubble interactions in aqueous solutions by atomic force microscopy: Effect of particle hydrophobicity. Colloids and Surfaces A: Physicochemical and Engineering Aspects, 300(3), 293–299. https://doi.org/10.1016/j.colsurfa.2007.02.003

15. Johnson, D. J., Miles, N. J., & Hilal, N. (2006). Quantification of particle–bubble interactions using atomic force microscopy: A Review. Advances in Colloid and Interface Science, 127(2), 67–81. https://doi.org/10.1016/j.cis.2006.11.005
16. Liu, T. Y., & Schwarz, M. P. (2009). CFD-based modeling of bubble-particle collision efficiency with mobile bubble surface in a turbulent environment. International Journal of Mineral Processing, 90(1-4), 45–55. https://doi.org/10.1016/j.minpro.2008.10.004
17. Lu, S. (1991). Hydrophobic interaction in flocculation and flotation 3. Role of hydrophobic interaction in particle—bubble attachment. Colloids and Surfaces, 57(1), 73–81. https://doi.org/10.1016/0166-6622(91)80181-m
18. Maxwell, R., Ata, S., Wanless, E. J., & Moreno-Atanasio, R. (2012). Computer simulations of particle–bubble interactions and particle sliding using discrete element method. Journal of Colloid and Interface Science, 381(1), 1–10. https://doi.org/10.1016/j.jcis.2012.05.021
19. Movasat, M., Cruz, A. D., & Tomac, I. (2023). Role of hydrophobic sand particle granularity on water droplet post-impact dynamics. International Journal of Multiphase Flow, 167, 104529. https://doi.org/10.1016/j.ijmultiphaseflow.2023.104529
20. Nguyen, A. V., Schulze, H. J., & Ralston, J. (1997). Elementary steps in particle—bubble attachment. International Journal of Mineral Processing, 51(1-4), 183–195. https://doi.org/10.1016/s0301-7516(97)00030-6
21. Nguyen, A. V., & Evans, G. M. (2002a). The liquid flow force on a particle in the bubble–particle interaction in flotation. Journal of Colloid and Interface Science, 246(1), 100–104. https://doi.org/10.1006/jcis.2001.8010
22. Nguyen, A. V., & Evans, G. M. (2002b). Axisymmetric approach of a solid sphere toward a non-deformable planar slip interface in the normal stagnation flow—

development of global rational approximations for resistance coefficients. International Journal of Multiphase Flow, 28(8), 1369–1380. https://doi.org/10.1016/s0301-9322(02)00025-3

23. Phan, C. M., Nguyen, A. V., Miller, J. D., Evans, G. M., & Jameson, G. J. (2003). Investigations of bubble–particle interactions. International Journal of Mineral Processing, 72(1-4), 239–254. https://doi.org/10.1016/s0301-7516(03)00102-9
24. Preuss, M., & Butt, H.-J. (1998). Direct measurement of particle−bubble interactions in aqueous electrolyte: dependence on surfactant. Langmuir, 14(12), 3164–3174. https://doi.org/10.1021/la971349b
25. Pyke, B., Fornasiero, D., & Ralston, J. (2003). Bubble particle heterocoagulation under turbulent conditions. Journal of Colloid and Interface Science, 265(1), 141–151. https://doi.org/10.1016/s0021-9797(03)00345-x
26. Ralston, J., & Dukhin, S. S. (1999). The interaction between particles and bubbles. Colloids and Surfaces A: Physicochemical and Engineering Aspects, 151(1–2), 3–14. https://doi.org/10.1016/s0927-7757(98)00642-6
27. Shi, L., Hu, C., Bai, M., &Lv, J. (2019). Molecular dynamics study on drag reduction mechanism of nonwetting surfaces. Computational Materials Science, 170, 109127. https://doi.org/10.1016/j.commatsci.2019.109127
28. Schulze, H. J. (1982). Dimensionless number and approximate calculation of the upper particle size of floatability in flotation machines. International Journal of Mineral Processing, 9(4), 321–328. https://doi.org/10.1016/0301-7516(82)90038-2
29. Schulze, H. J. (1989). Hydrodynamics of bubble-mineral particle collisions. Mineral Processing and Extractive Metallurgy Review, 5(1-4), 43–76. https://doi.org/10.1080/08827508908952644

30. Sutherland, K. L. (1948). Physical chemistry of flotation. XI. Kinetics of the flotation process. The Journal of Physical and Colloid Chemistry, 52(2), 394–425. https://doi.org/10.1021/j150458a013

31. Tao, D. (2005). Role of bubble size in flotation of coarse and fine particles—a review. Separation Science and Technology, 39(4), 741–760. https://doi.org/10.1081/ss-120028444

32. Verrelli, D. I., Koh, P. T. L., & Nguyen, A. V. (2011). Particle–bubble interaction and attachment in flotation. Chemical Engineering Science, 66(23), 5910–5921. https://doi.org/10.1016/j.ces.2011.08.016

33. Wang, G., Evans, G. M., & Jameson, G. J. (2016a). Bubble–particle detachment in a turbulent Vortex I: Experimental. Minerals Engineering, 92, 196–207. https://doi.org/10.1016/j.mineng.2016.03.011

34. Wang, G., Nguyen, A. V., Mitra, S., Joshi, J. B., Jameson, G. J., & Evans, G. M. (2016b). A review of the mechanisms and models of bubble-particle detachment in froth flotation. Separation and Purification Technology, 170, 155–172. https://doi.org/10.1016/j.seppur.2016.06.041